Capillary imbibition depth in particle-bed 3D printing – Physical frame and one-dimensional experiments

Wenqiang Zuo, Chenghao Dong, Patrick Belin, Nicolas Roussel, Emmanuel Keita

Capillary imbibition depth in particle-bed 3D printing – physical frame and one-dimensional experiments

Wenqiang Zuo, Chenghao Dong, Patrick Belin, Nicolas Roussel*, Emmanuel Keita*

Navier Laboratory, Gustave Eiffe Universityl, ENPC, CNRS, Marne-la-Vallée, France

Corresponding author: nicolas.roussel@ifsttar.fr

Corresponding author: emmanuel.keita@univ-eiifel.fr

Abstract

This paper deals with the control of the net geometry of a printed object in the case of powder-bed or particle bed binding technologies. We first measure and compare water penetration in one-dimensional experiments for various powder-beds. Our results, despite the simplicity of the experimental set-up, show a feature that has not been reported in literature so far, namely the fact that water penetration depth is not finite but is fully uncontrolled on longer time scales. We discuss the physical origin of this feature and the reasons why it is hidden by other aspects in most papers or applications. We finally show that water penetration depth can be controlled by a dispersed organic water thickener. Our results suggest the formation of a non-Newtonian fluid between the binder grains, which allows, in turn, for the control of the naturally uncontrolled capillary-driven water penetration in the powder-bed.

Keywords: Powder-bed; 3D Printing; Penetration; Cement; Plaster; Thickeners

1. Introduction

Digital fabrication with concrete emerged at the end of the 20th century [1,2] and has since received widespread attention [3–9]. This technology integrates computer-aided design with automated production processes in the production of construction objects [3]. Additive Manufacturing (AM) is a class of Digital fabrication that consists in manufacturing layer-by-layer cement-based materials [5,6]. Various AM techniques exist as classified in [10], including particle-bed binding, material extrusion, and material jetting. Particle-bed binding adopts selective powder activation by liquid jetting to bind the particle bed layer-by-layer [6,11–16]. After printing, the unreacted particles [6] are removed to retrieve the printed object. This technology allows for the processing of real three dimensional complex shapes with a high resolution of the order of the constitutive powder size.

From a material point of view, two particle-bed binding technologies are currently developed. The first solution (sand-bed 3D printing) uses an inert sand particles bed and a liquid binder made of cement or plaster and water [11]. The second solution (powder-bed 3D printing) consists in spraying a solvent (water) on a reactive powder made of a binder (cement, plaster) and potentially a sand [17,18].

Dimensional accuracy is, similarly to other digital processing technologies, one of the main concerns of powder bed 3D printing techniques. While the printing accuracy is influenced by the size of the particles, it is mainly driven by the behavior (at contact and during penetration) of the droplets of water deposited or projected at the surface of the reactive binder. Besides, the process may also be kept under control by the competition of the imbibition and the setting kinetics.

In the current work, we study the penetration of water in various powder-beds. In pure cement powder-bed and pure plaster powder-bed, we show that capillary-driven water penetration is fully uncontrolled and is therefore not expected to be directly compatible with industrial 3D printing applications. Our results suggest that

the use of water thickeners dispersed in a given powder-bed for a given water droplet allows for the control of the naturally uncontrolled capillary-driven liquid water penetration through the progressive formation of a non-Newtonian fluid between the powder grains.

2. Background and research significance

When a water droplet of diameter d, volumic mass ρ and surface tension γ hits a solid non-permeable surface, the droplet either splashes or coats the surface. In very rare and specific conditions, it might bounce off [19]. Typical water spraying systems result in droplet velocities V of the order of 1 m/s. If the droplet kinetic energy density, of order ρV^2, is much higher than capillary pressure of order γ/d, the droplet splashes when hitting the surface. For typical values of surface tension around $\gamma \approx$ 0.05 Pa.m, this is expected to only happen for sprayed droplets larger than 1 mm. As a consequence, most spraying devices in powder bed printing will deliver droplets that do coat the surface and do not splash. Obviously, devices delivering a low velocity constant stream (or jet) of liquid (*i.e.* not spraying) will also coat the surface as long as the local liquid pressure does not reach the cohesion limit of the powder bed.

The surface of the powder bed is however permeable and the coating process is driven therefore by the competition between the droplet (or liquid stream) viscous spreading as usually described by Tanner's law [20] and capillary imbibition (see Fig. 1).

The two features in Fig. 1 despite their major influence on the geometric accuracy of the printing process have not been studied in details in the case of cement or plaster powder beds, where both spreading/coating and imbibition on medium to long time scales are expected to potentially compete with hydration and vary with the physical properties of the particles bed.

We choose here to decorrelate the two above features for the sake of simplicity and choose to focus this study on capillary imbition only using the simple one-

dimensional experiments described in the next section.

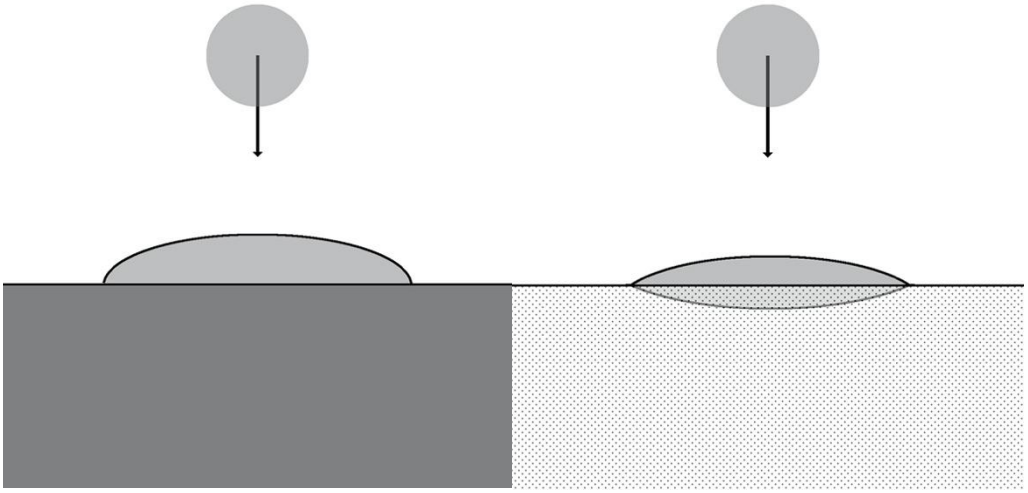

Fig. 1. *Coating of a surface by a non-splashing liquid droplet. (Left) non permeable surface – coating only (right) permeable surface – coating and imbibition occur simultaneously.*

From a practical point of view, for a robust and repeatable geometry control of powder bed binding techniques, the liquid projected or deposited on the surface of the powder bed is expected (and assumed) to diffuse inside the powder over a well-controlled length [6,11,17,21]. In literature, process parameters such as droplet mass, pressure, particle layer thickness, particle composition and packing properties [6,18,22,23] were all reported to play an essential role in geometry control.

From a theoretical point of view, the liquid penetration length is driven by the capillary diffusion of a Newtonian liquid in a porous particle bed. Within this frame, the liquid is excepted to be free to diffuse in the dry powder under the effect of capillary suction [6,11,24]. Most powder beds contain powders with binder particles around 10 micrometers. As a consequence, the typical powder bed pore size r is expected to be of the order of the size of the constitutive particles, namely around 10 micrometers. This suggests that the capillary suction is around γ/d, namely around 10^4 Pa. This pressure is far higher than any gravity induced stress at the level of one powder layer. With hydrostatic pressure $\rho g H$ around 10^2 Pa for centimetric layers, hydrostatic pressure influence on short time scales imbibition can therefore

be neglected.

Please note that, within the present study, any external pressure applied to the liquid, such as the one induced by applying a liquid jet, will be neglected. This assumption holds true as long as the liquid external pressure stays lower than capillary suction, namely 10^4 Pa.

2. Materials and methods

2.1. Powder characterization

Three powders are used in this study: a CEM I Cement (Lagerdorf, Lafarge) with a density of 3150 kg/m^3; a plaster (Molda 3 Normal, Formula Saint-Gobain) with a density of 2630 kg/m^3; and a 3D printing plaster powder (3DP Plaster) obtained from a printer manufacturer (PXL Core, Z-Corp) with a density of 2530 kg/m^3. The main components of the 3D printing plaster powder are calcium sulfate hemihydrate (80%-90% by weight), vinyl polymer and carbohydrate [25]. The particle size distribution of each powder was measured with a laser particle size analyzer (Malvern Mastersizer S) after dispersion in isopropanol (see **Fig. 2**Erreur ! Source du renvoi introuvable.). The median particle sizes of the cement powder, the plaster powder and the 3DP Plaster powder are around 11.5 µm, 12.5 µm and 35 µm, respectively.

A hydroxy ethoxy methoxy cellulose (HEMC) was used as a water thickener in the cement powder bed system. The HEMC is used in powder form. The constitutive macro-molecules have a molar mass of 370,000 g/mol and a density of 1200 kg/m^3. The radius of HEMC in dilute regime was measured to be around 39 nm using Dynamic Light Scattering [26]. The polymer overlapping concentration c^* of HEMC is around 0.3%. More details about this polymer can be found in a previous work where this polymer is noted as HEMC A [26]. The mass ratio of HEMC to cement ranges from 0% to 8%. For the preparation of the powder-bed containing both cement powder and HEMC, dry cement powder and the HEMC powder were mixed for 30 minutes in a planetary mixer to achieve homogeneity.

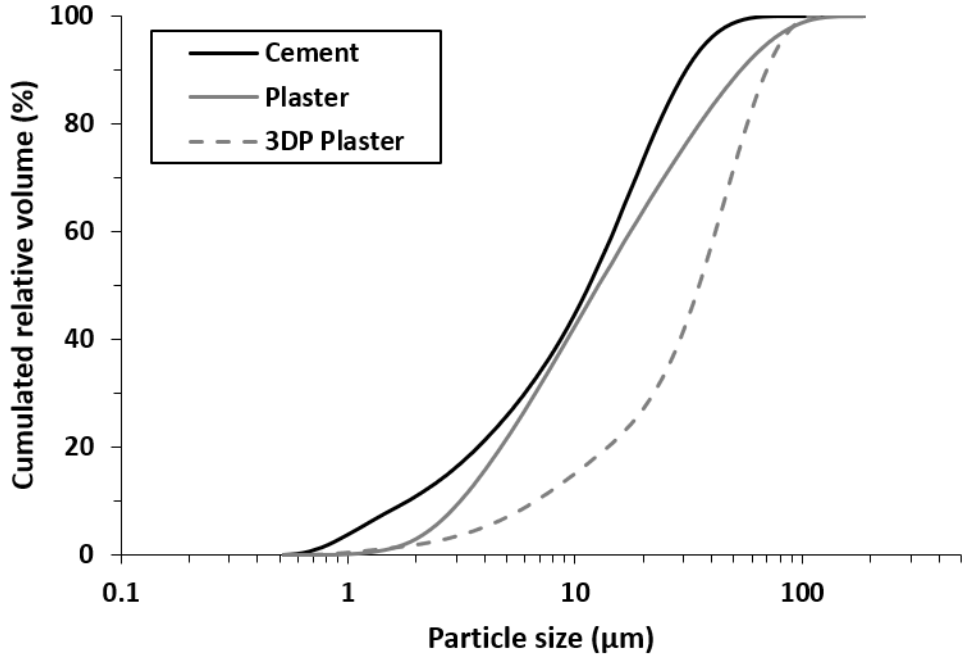

Fig. 2. *Cumulative particle size distribution of the cement powder and the plaster powder used in this study.*

The packing fraction of the powder-beds (*i.e.*, the volume of solid by unit of total volume) was assessed by measuring the mass of powder in a reference container. The measured packing fractions of cement (with or without HEMC), plaster, and 3DP plaster powders were all 40 ± 2%. Packing density was checked before each experiment after preparation of the powder bed.

In order to assess the potential water consumption induced by ongoing chemical reactions, a thermocouple was embedded in sealed plastic containers (5.2 cm in diameter and 7.0 cm in height). The containers were filled with fresh cement paste (water-to-powder mass ratio w/p = 0.4), plaster paste (w/p = 0.6) and 3D printing plaster paste (w/p = 0.6). A distinct temperature increase, which denotes the onset of the acceleration period [27], was recorded after 2 min, 20 min and 200 min for 3D printing plaster paste, plaster paste, and cement paste, respectively. A peak in temperature was then measured at 15 min, 60 min, and 600 min for 3D printing plaster paste, plaster paste, and cement paste, respectively (see **Fig. 3**).

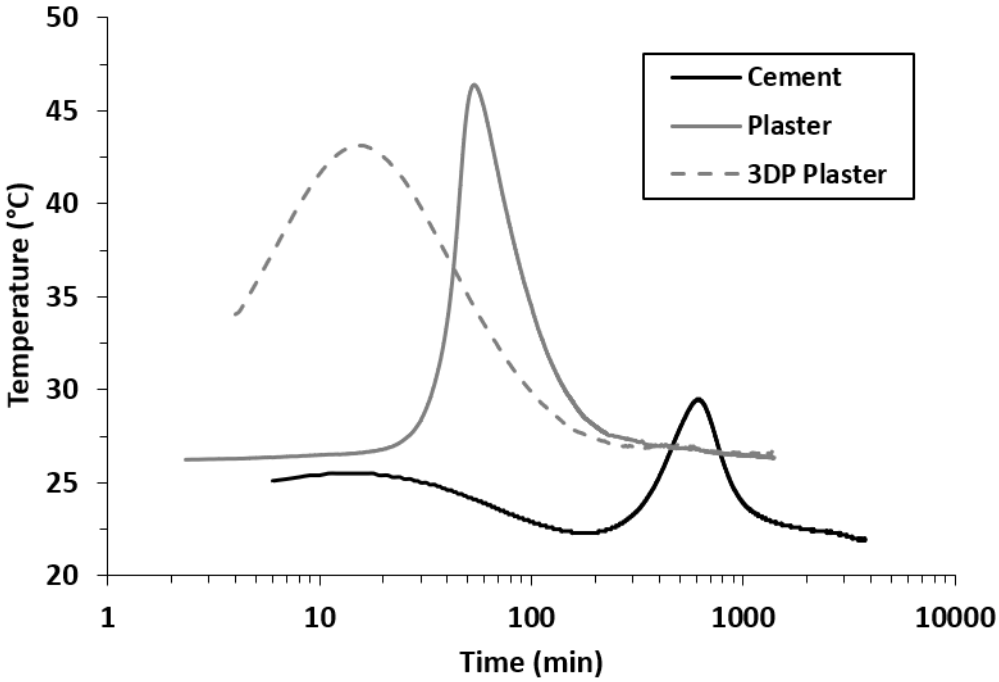

Fig. 3. *Temperature variation during hydration as a function of time for the three binders studied here.*

2.2. Liquid characterization

In order to assess the viscosity of the interstitial solution formed upon penetration into the cement powder mixed with HEMC, solutions with different HEMC dosages were independently prepared. HEMC dry powders were slowly added to a beaker containing deionized water. A magnetic stirrer was used to disperse the solution for 24 h. A C-VOR Bohlin stress-controlled rheometer with serrated parallel plates (diameter = 40 mm, gap = 0.5 mm) was then used to assess the rheological properties of the solutions. An increasing shear rate ramp from 0.01 s^{-1} to 100 s^{-1} was applied for 1000 s (with a logarithmic distribution of shear rates) followed by a decreasing shear rate ramp for 1000 s. Only the decreasing ramps are analyzed in the following.

Typical rheological measurements of these solutions are plotted in **Fig. 4 (a)**. For solutions with HEMC concentration lower than 2%, a Newtonian behavior was systematically measured. We noted that the solution behavior gradually switches to a shear-thinning behavior at high shear rates as the HEMC concentration becomes

higher than the overlapping concentration c^* given above. For solutions with HEMC concentrations higher than 4%, a yield stress fluid behavior was measured. It finds its origin in the formation of an entangled polymer network above a second critical concentration noted c^{**} [28,29]. The yield stress of these HEMC solutions is extrapolated from a Herschel–Bulkley model fitting at low shear rates (see **Fig. 4 (a)**).

The apparent viscosity of the solutions (*i.e.*, the ratio between the shear stress and the shear rate) is plotted at a shear rate of 1 s^{-1} in **Fig. 4 (b)**. The viscosity increases sharply from 1 mPa· s to several thousands of Pa· s as the HEMC concentration increases from 0% to 10% (see **Fig. 4 (b)**).

We then plot in **Fig. 4 (c)** the yield stress as a function of HEMC concentration. In the range of dosages studied in this work, the yield stress of the solutions increases gradually up to 30 Pa.

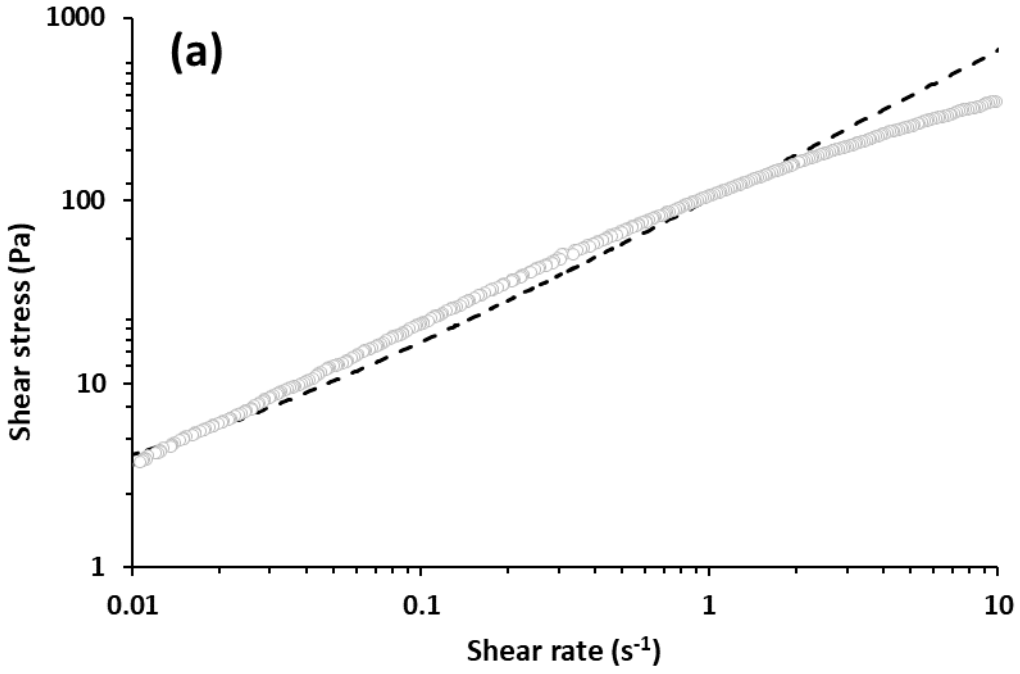

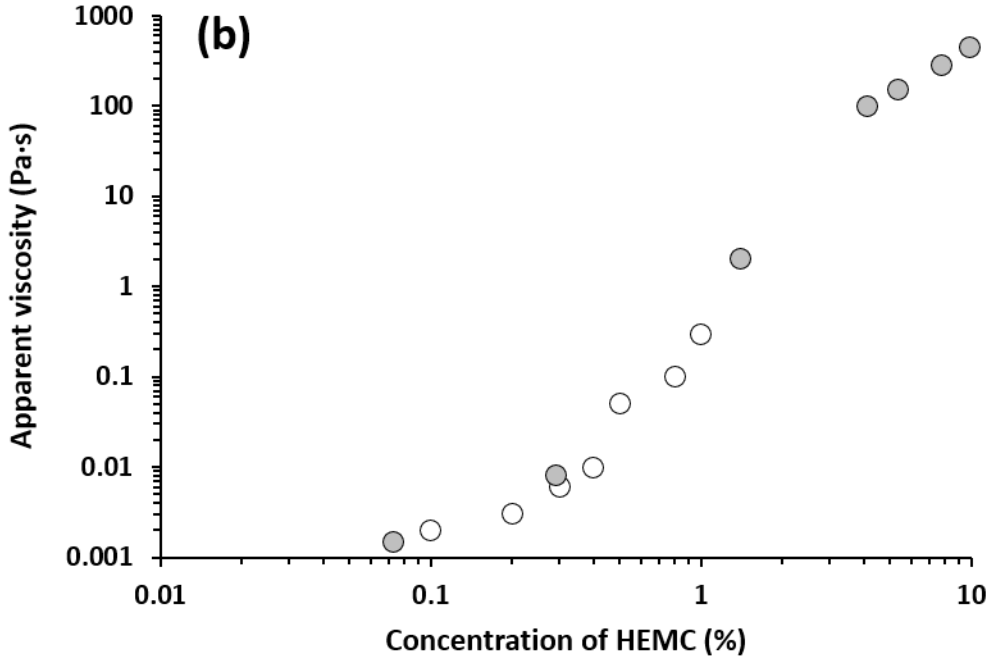

184

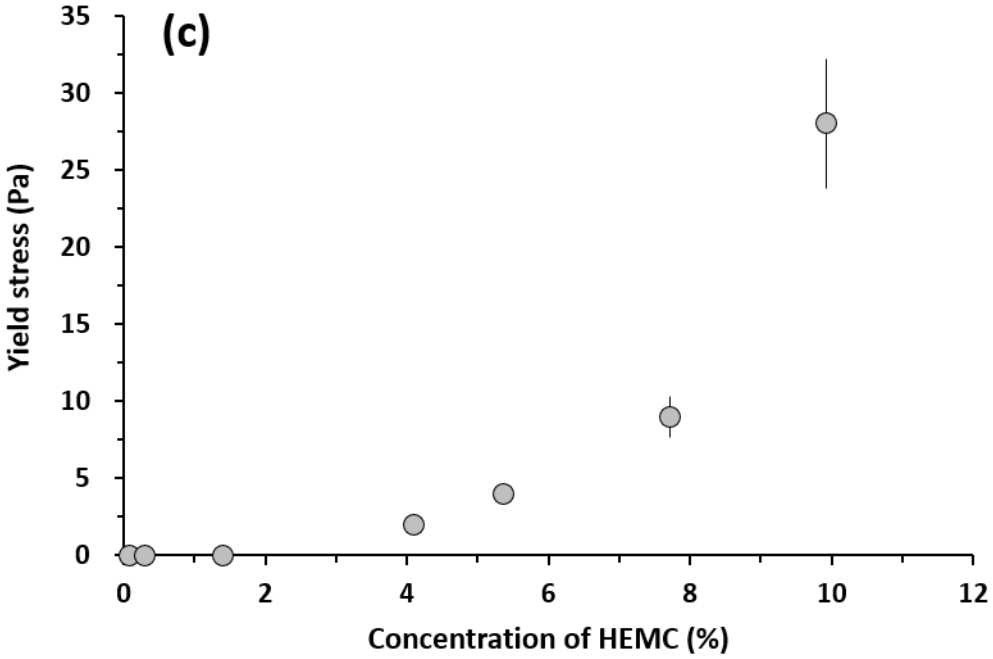

185

186 ***Fig. 4***. *Rheological properties for solutions with different HEMC concentrations: (a)*
187 *Shear stress as a function of shear rate for a solution of 4% HEMC in water (circles).*
188 *The dash line is the Herschel–Bulkley model fit used to extrapolate yield stress; (b)*
189 *Apparent viscosity at 1 s-1 as a function of HEMC concentration (white circles are*
190 *results from a previous study [26]); (c) Yield stress as a function of HEMC*
191 *concentration.*

192

193

194 **2.3. One-dimensional water penetration measurements**

195 As discussed in the background section, a one-dimensional penetration experiment
196 was designed to assess liquid penetration in the powder bed. The powder was
197 packed into glass tubes with an inner diameter of 10.5 mm and a height of 10 cm.
198 The bottom of the tubes was cut off by a wire cutter and sealed with filter paper. This
199 allows air to escape from the bottom during liquid penetration. The tubes were filled
200 up to 7 cm and gently vibrated to obtain both a flat top-surface of the bed and to
201 achieve the packing fraction mentioned in **section 2.1**. Then, 0.4 mL of distilled water
202 was added within 1 second on the top-surface of powder-bed using a high-
203 performance micro-pipette (see **Fig. 5**). The tubes were then sealed to avoid any
204 evaporation. The above amount of water corresponds theoretically to a water layer
205 of thickness around 5 mm before penetration. A digital camera was then used to
206 record the penetration depth of the liquid. Comparing the water level above the
207 surface and the penetration depth in the powder bed and accounting for the porosity
208 to be filed by water, we concluded that wall effects are negligible in our experiments
209 (results not shown here). Some penetration fronts were noted to be non horizontal,
210 which may be due to the heterogeneity of the pore size distribution. The penetration
211 depths of the liquid reported in this work were therefore computed by averaging
212 three measurements, *i.e.*, left, middle, and right of each tube picture at each
213 recording time (see arrows in **Fig. 5**). We moreover checked the repeatibility of our
214 measurements (see **Fig. 6**). All measurements were carried out at room temperature
215 (22 ± 1℃).

216

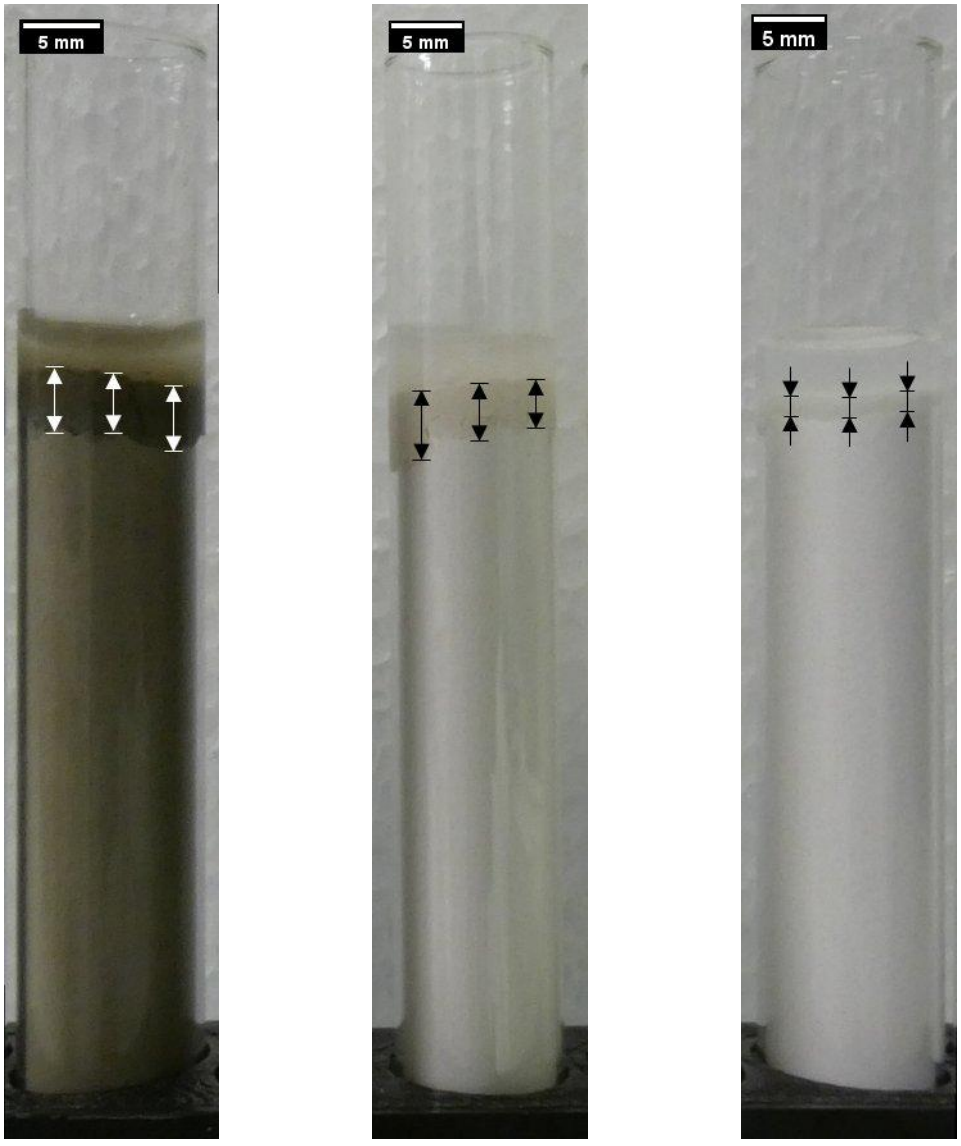

(a) (b) (c)

Fig. 5. *One-dimension measurement of water penetration in powder-beds: (a) cement powder; (b) plaster powder; (c) 3DP plaster powder. The arrows stand for the depth of the liquid that has penetrated in powder-bed. Note: the images shown here were taken 30 s to 1 min after water addition.*

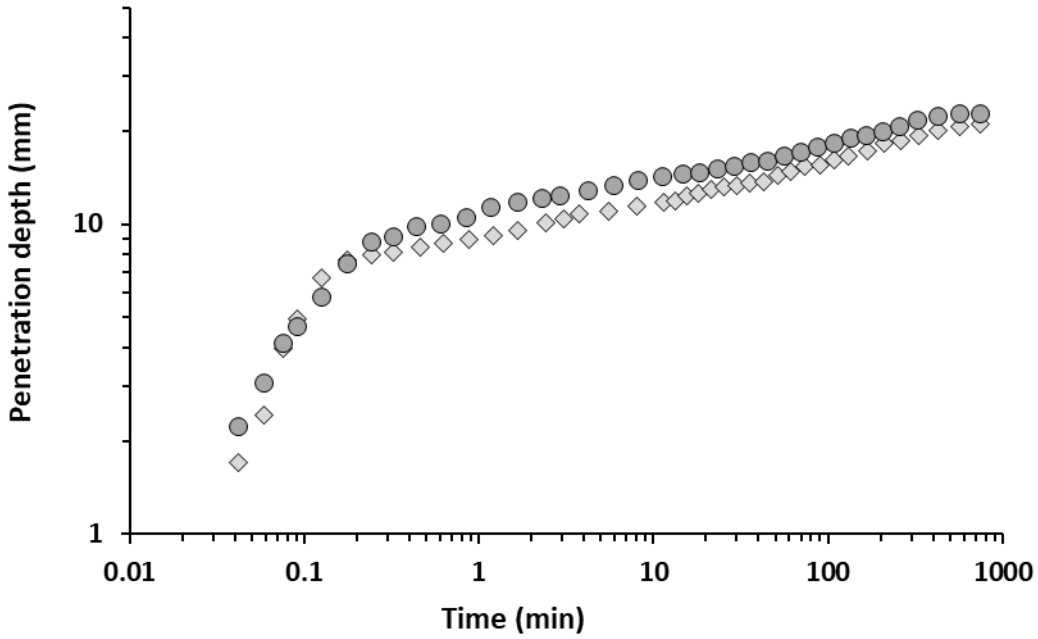

Fig. 6. *Repetition of the one-dimensional measurement for pure cement powder-bed with a solid volume fraction of 40% and a 0.4 ml water addition.*

3. Penetration of water in plaster powder bed and cement powder bed

3.1. Experimental results

We first show in **Fig. 7** the measured water penetration depth as a function of time for plaster powder-bed, cement powder-bed and commercial 3DP Plaster powder-bed. The water penetration depths in plaster and cement powders show similar trends. They initially increase with the square root of time for around 1 min and slow down sharply afterward. The transition occurs for a penetration depth around 7 mm. This depth corresponds to the so-called “saturation penetration depth” computed by assuming that the initial water on top of the sample has fully penetrated and has saturated the porosity of the powder bed (see the fine dash line in **Fig. 7**). It means that, as soon the available water has fully filled the available porosity, the initial fast penetration regime ends.

However, capillary imbibition does not stop when water has fully invaded the porosity. The interesting feature to be kept in mind from **Fig. 7** is that, after the initial fast penetration of around 7 mm in one minute, water penetration depth more than

doubles over the following 100 minutes. This evolution scales with the power 1/8th of time as indicated in **Fig. 7** (this observation will be studied in a further study). As a consequence, the liquid saturation in the powder bed porosity drops down from 100% at 1 minute to 50% at 100 minutes.

We then note that hydration onset does not affect water penetration kinetics (Cf. star symbols in **Fig. 7**). However, around the time of the hydration peak of plaster and cement from **Fig. 3**, the water penetration front gradually vanishes preventing any further measurements (see **Fig. 7**).

Finally, we note that water penetration depth in the commercial 3DP plaster powder is far lower than the ones measured in the two other types of powder despite the fact that all powder beds have the same packing fraction and therefore porosity.

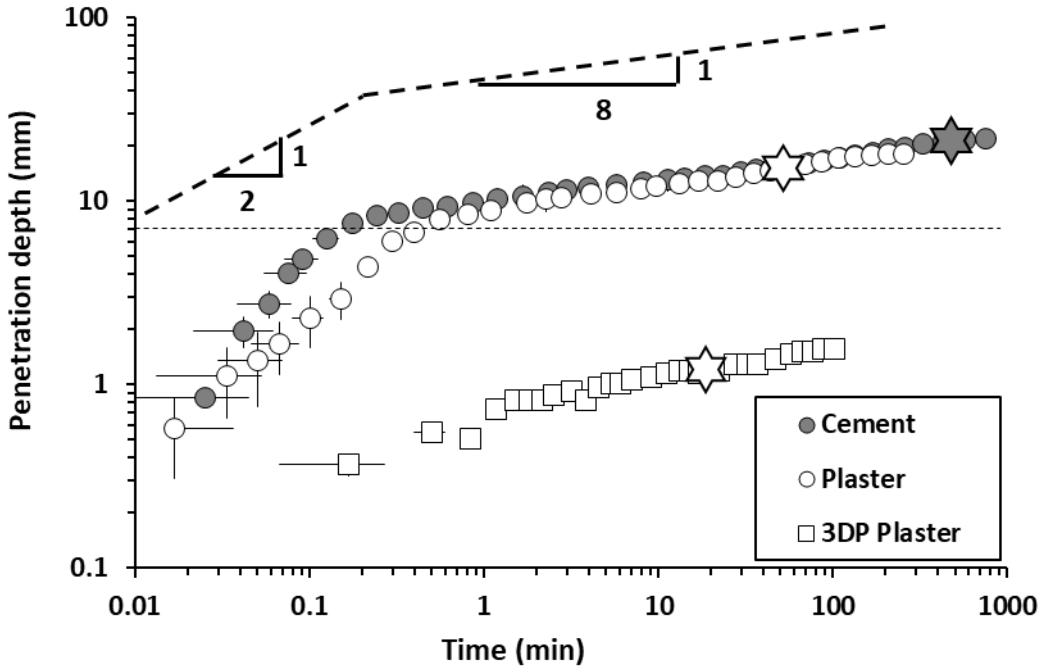

Fig. 7. *Water penetration depth in powder-beds as a function of time. The dash lines stand for the scaling relationship between penetration depth and time. The fine horizontal dash line stands for the saturated penetration depth (Cf. text for definition), and the stars on each curve stand for the time of hydration peak.*

3.2. Discussion

3.2.1 Saturated penetration

According to Washburn's law, as long there exists a reservoir of water above the surface, water penetration depth h_s can be written as [30]:

$$h_s = \sqrt{\frac{k_0 P_{cap} t}{2\mu}} \quad \textbf{(1)}$$

where μ is the liquid viscosity. The permeability k_0 of the porous medium, can be estimated using the Kozeny-Carman formula $k_0 = \frac{\omega^3}{45(1-\omega)^2} r^2$, where ω is the porosity and r is, as above, the pore radius [31,32]. P_{cap} is the capillary pressure already discussed above and is of the order of γ/r. It can be noted from **Eq. (1)** that water penetration depth in the powder-bed is expected to scale with the square root of time. Interestingly, this is the case for both the plaster powder-bed and the cement powder-bed, but not for the commercial 3DP Plaster powder (see **Fig. 7**).

3.2.2 Unsaturated penetration

When there is no water left above the surface, the saturated powder is expected to desaturate progressively as water penetration goes on. As a decrease in saturation leads to a decrease in the liquid relative permeability [33], water penetration kinetics is expected to slow down (see **Fig. 7**). This decrease in permeability, and therefore the slowing down of the water penetration velocity under the constant capillary pressure, will go on. This decrease is expected to stop when the liquid saturation in the porosity reaches a critical saturation level, below which the liquid network in the porosity is expected to disconnect [34]. At this latter stage, water displacement may only occur through vapor transfers, which are orders of magnitude slower. Typical values for this critical saturation level are of the order of 5%. This suggests that, on long time-scales, water may travel over distances 20 times longer than the saturation depth discussed in the previous section.

This long time-scales propagation of water may be a major issue if the onset of the hydration reaction is slow. Indeed, during the dormant period, this long-range water propagation may bring the water saturation level below the amount required for proper cement hydration.

However, this feature has not been, up to the authors' knowledge, ever discussed, reported or even measured in the cement-based literature so far. Propagation depth of water is always assumed to be a finite value and it is always assumed that there is locally enough water for the binder hydration when it occurs.

A first reason could be hydration itself. Even if the onset of hydration does not affect the unsaturated propagation of water as shown in **Fig. 7**., the hydration peak is expected to consume enough water locally to bring saturation below the critical saturation level defined above and stop any further water propagation. If this happens not too long after the end of the saturated propagation regime, the water propagation length could then appear as finite and constant.

However, particle bed printing is, more than often, carried out, on non-accelerated systems where the hydration peak only occurs after several hours. In these cases, another explanation could be found in the lower permeabilities of the powder beds used in real printing when compared to the pure powder beds studied here. If we consider that 50% of the powder volume is often substituted by sand, we can expect the packing fraction of the bed to increase from the measured value of 40% (see section 2.1.) up to 70%. The porosity would, in turn, drop from 60% to 30% and the permeability would scale down by a factor 5 according to the analytical approach proposed by Perrot *et al*. [35,36]. As a consequence, the "fast" saturated penetration regime would then last 5 times longer (*i.e.* of the order of ten minutes) and the further unsaturated water penetration length before the hydration peak would then become much shorter. The penetration depth would then be finite and well-controlled and there would locally be enough water for the binder hydration.

Such a feature would however prevent from powder printing based on pure powders (i.e. without any coarser particles allowing for a decrease in porosity and permeability). Nevertheless, several authors in literature have carried out some

317 powders printing on pure metakaolin powders without encountering any specific
318 issues regarding the activation liquor penetration depth [16]. However, while these
319 activation liquors (sodium silicates or potassium silicates) have similar surface
320 tension values as water, they have viscosities one or two orders of magnitudes higher.
321 Once again, as the penetration kinetics of this high viscosity liquid is slower, it
322 becomes easier to reach a finite and well-controlled liquid penetration by ending it
323 with a chemical reaction.
324

325 ## 4. Penetration of water in powder-beds containing thickeners

326 ### 4.1. Experimental results

327 We plot in **Fig. 8** the measured water penetration depth as a function of time
328 for various HEMC dosages.

329 For dosages lower than around 1%, the curves are similar to the ones obtained
330 previously on powder beds not containing any HEMCs with a saturated penetration
331 regime followed by an unsaturated penetration regime. The water penetration depth
332 kinetics are however slower (Cf. the 0.2% HEMC dosage curve in **Fig. 8**)

333 For dosages higher than around 1%, the water penetration depth follows a
334 different trend than the one measured previously. In a first saturated penetration
335 regime, the penetration depth increases quickly and then stops. On longer time
336 scales, water penetration depth barely changes. The time and penetration depth at
337 which penetration stops both decrease with increasing HEMC dosage. It can
338 moreover be noted that, for these dosages, some residual water on top of the
339 surface can be visually assessed. This result is in contrast with the idea that water
340 continuously propagates in the sample under the effect of capillary suction. This, in
341 turn, suggest that something able to compete with capillary forces prevents the
342 water from moving. As a consequence, the water penetration depth becomes finite
343 and is correlated to the thickener's dosage as shown in **Fig. 9**.

344 We suggest, in the following, that the dissolution in the penetrating liquid of the
345 thickener dispersed in the powder bed is able to provide the penetrating water with

346 a yield stress, which, in turn, is able to prevent the water from propagating despite
347 capillary suction.
348

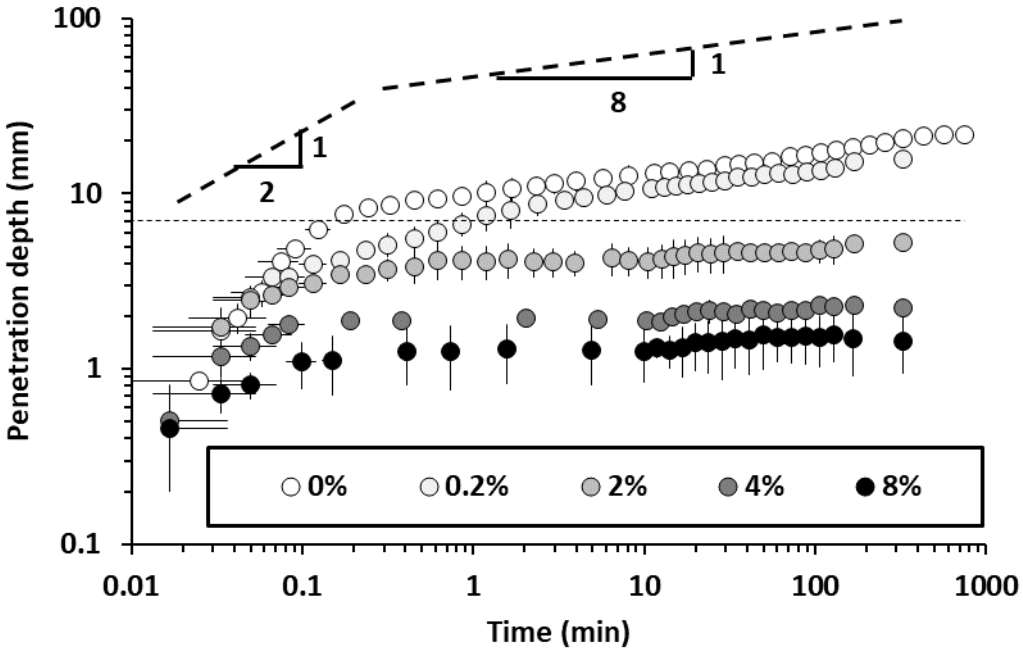

349
350 ***Fig. 8.*** *Penetration depth as a function of time for powder-bed containing different*
351 *HEMC dosages. The numbers in the legend stand for the mass ratios of HEMC to*
352 *cement, the bold dash lines stand for the scaling relationship between penetration*
353 *depth and time, and the fine dash line stands for the saturated penetration depth*
354 *after which the system is unsaturated.*
355

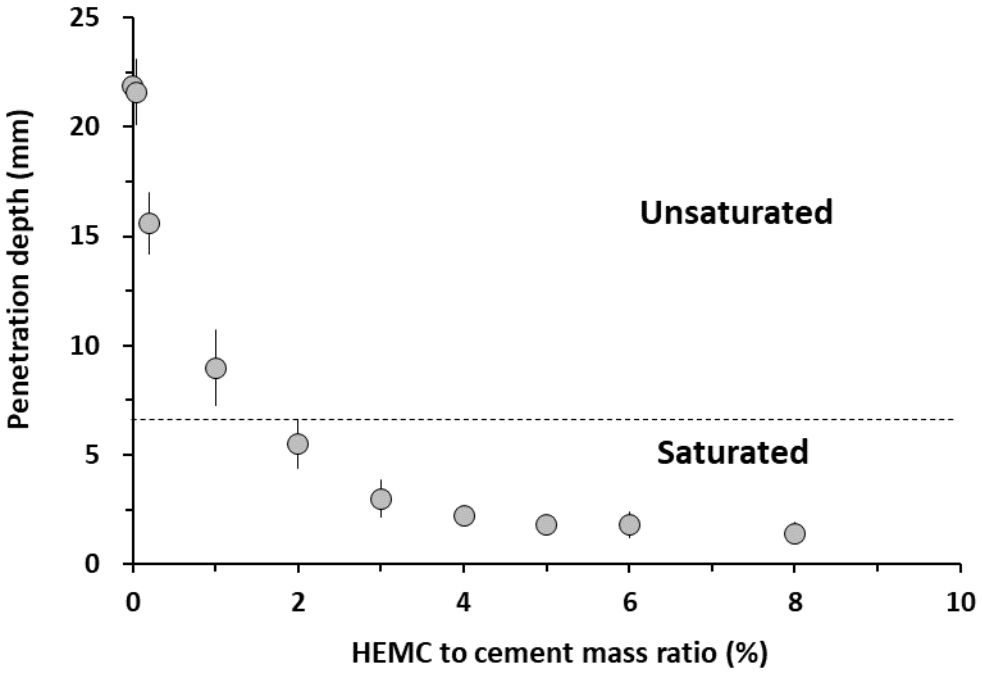

Fig. 9. *Penetration depth after 200 minutes as a function of HEMC content in the cement powder bed. The dash line stands for the water penetration depth, above which the system becomes unsaturated.*

4.2. Discussion

We assume in a first step that the HEMC gets fully dissolved in the penetrating water upon contact. This assumption allows for the computation of the HEMC concentration as a function of penetration depth. In the saturated penetration regime, the concentration is expected to be constant and proportional to the HEMC dosage in the powder bed while, in the unsaturated penetration regime, this concentration is expected to increase with penetration depth. Indeed, the total amount of water in the powder bed stays constant while the depth of the invaded porous zone and the potentially dissolved HEMC amount both increase.

Let us first focus on the saturated penetration regime that applies to all the highest dosages of HEMC in **Fig. 8** and **Fig. 9**. According to the analytical frame of Pierre et al [11,37], a yield stress fluid penetration in a powder bed is expected to stop at a depth H where the capillary pressure gradient $\nabla P/H$ equilibrates the stress gradient τ_c/d_p[11]. d_p is the particle diameter and τ_c is the yield stress of the

375 penetrating fluid. Therefore, the penetration depth of a yield stress fluid in a powder-
376 bed is expected to scale as [11]:

$$H = \frac{d_p P_{cap}}{\alpha + 6\kappa(1-\omega)/\omega} \cdot \frac{1}{\tau_c} \quad \textbf{(2)}$$

377 where κ captures the fraction of the powder grains surface area where the fluid is
378 sheared. It is assumed to be equal to 1 when penetration is homogeneous. α is a
379 dimensionless geometrical fitting parameter reported to equal 5.5 in [10].

380 We plot the penetration depth measured here as a function of the predicted
381 penetration depth according to **Eq. (2)** in **Fig. 10**. To do so, we use the yield stress
382 values from **Fig. 4 (c)**. The predicted penetration depth is in rather good agreement
383 with the measured one. This suggests that, at first order, one can consider that all
384 HEMC particles are immediately dissolved in the penetrating liquid [38,39] and that
385 the influence of HEC on the capillary suction is neglectable. It could however be
386 objected that the higher penetration depths (compared to predicted ones) measured
387 at lower dosages in **Fig. 10** are the traces of a delay in the dissolution the thickener
388 while the lower penetration depth measured at the highest dosage suggests that the
389 thickener dissolution is not complete. It can however be inferred that, for a system
390 that stays saturated, penetration depth scales at first order with the inverse of the
391 yield stress of the penetrating fluid. We suggest that this feature explains the lower
392 penetration depth measured in the case of the commercial plaster in **Fig. 7**. Total
393 Organic Carbon (TOC) measurements carried out on this powder revealed the
394 presence of a high amount of organic compound (results not shown here) that we
395 suggest to be the signal for a thickener addition.
396

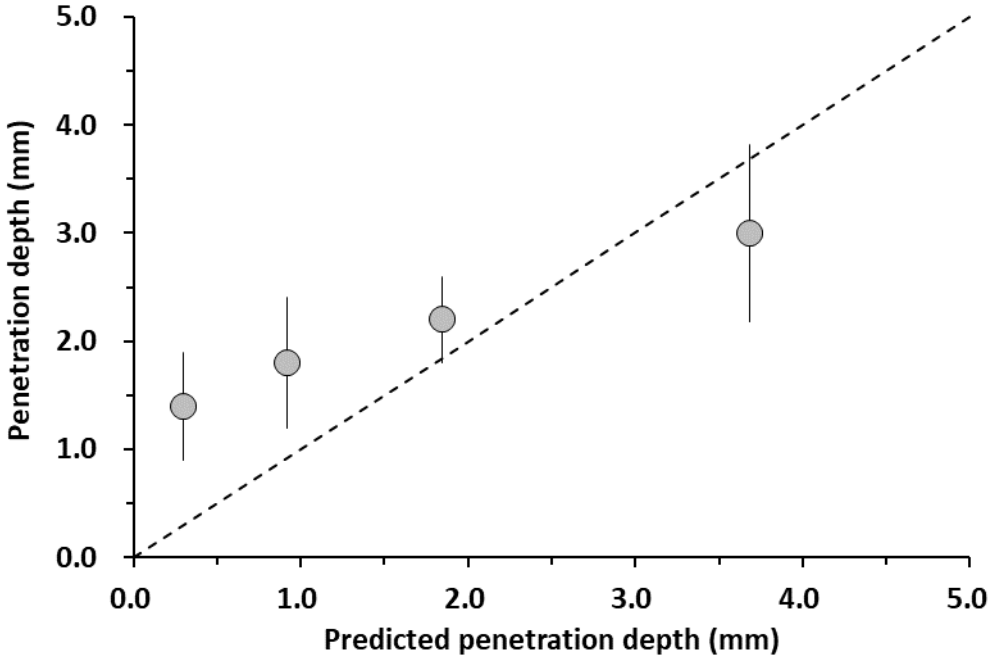

Fig. 10. *Experimental penetration depth for HEMC concentration above 3% and predicted penetration depth (see* ***Eq. (2)****). The black dash line stands for y = x.*

For the powder beds that reach the unsaturated regime, the resulting HEMC effective dosage in the penetrating liquid is expected to be proportional to the penetration depth leading to a progressive change in the penetrating liquid rheological properties. For the lowest HEMC dosages, it is unlikely that they develop a yield stress fluid on the time scale of the experiment (*e.g.*, the case of HEMC dosage of 0.2% in **Fig. 8**). Consequently, the unsaturated penetration process follows the same steps as the one described or powder beds not containing any thickeners. It can however be expected that the penetration process is slowed down by the higher viscosity of the penetrating fluid resulting from the dissolution of the thickener. For higher HEMC dosages in the unsaturated regime, we suggest that, similarly to saturated regimes, the unsaturated penetration process stops as soon as a yield stress fluid is formed and balances the capillary-driven force as shown in **Eq. (2)**.

5. Shape control: morphology of liquid penetration zone

According to the above results and discussion, water penetration depth is naturally uncontrolled. It can however be controlled by dispersing a thickener into the powder bed. This means that the extent of the penetration zone during printing becomes tunable at will depending on the dosage of thickener in the powder bed. In practice, this dosage shall therefore be chosen so that there remains enough water in the porosity to fully hydrate the reactive powder in the penetrated zone. To illustrate this situation, we carry out the following experiments similarly to the ones from [16].

Water droplets of 20 µL (diameter around 3 mm) are deposited on the powder-bed surface using an ultra-high-performance micropipette. After penetration and setting, the resulting hardened zones in the bed are extracted from the unreacted powder using a sieve with a mesh size of 200 μm. This last step is carried out 12 h after the droplet deposition.

It can be noted that the typical penetration time of the droplets is around 1 min (visual observation), whereas, in this period, the water evaporation ratio (*i.e.* the ratio between evaporated water mass and droplet mass) always stays lower than 2% (data not shown here).

We show in **Fig. 11** the morphology of the resulting granules after setting and hardening as a function of CE dosage. It can be seen in **Fig. 11** that, the cement powder containing none or the lowest HEMC dosage (*i.e.*, the granule with 0.2% dosage of HEMC), the morphology of the hardened objects extracted from the unreacted powder is uncontrolled. The resulting object has a typical size far lower than the water penetration depth expected from the one-dimensional measurements of the previous sections (*i.e.*, the translucent cylinder in **Fig. 11**). We suggest that the slow unsaturated penetration regime shown in **Fig. 8** brings the water-to-cement ratio in most of the samples below the value required for hydration and grains binding.

Although one could print in this regime with a bit of experience and practice, it has to be noted that, in such conditions, recycling of the powder surrounding the printed object shall become an issue. Indeed, in this regime, the porosity of the

powder surrounding the extracted object will contain some water. It is expected therefore to be partially hydrated even though this hydration was not sufficient to bind the cement grains.

In the case of the cement powder containing 1 % dosage of HEMC in **Fig. 11**, it can be expected from the previous sections of this paper that unsaturated penetration occurs for a short period of time. It however stops as soon as a yield stress fluid appears due to the thickener dissolution and balances the capillary pressure. Therefore, the saturation level stays high enough to allow for proper hydration and binding of the cement grains. However, printing objects in this regime would potentially raise the issue of printing rate and productivity. Indeed, the above regime involves a slow unsaturated penetration process as shown in **Fig. 8**. The final shape, although controllable, will only be reached after a couple hours.

For the cement powder containing 4%, 6%, and 8% HEMC in **Fig. 11**, the shape of the granules that formed during liquid penetration is the one of regular disks. The influence of the coating (or spreading of the droplet) not studied in this work can clearly be seen. The thickness of these disks decreases with increasing HEMC dosage in the powder-bed. In this thickener dosage range, the penetration zone is expected to be saturated with liquid and hydration allows for the binding of the cement grains. The shape of the hardened granules can therefore be well-controlled. There however exists a risk of having an excess of water at the top of the powder bed if the deposition rate of water above the bed is not adequately chosen.

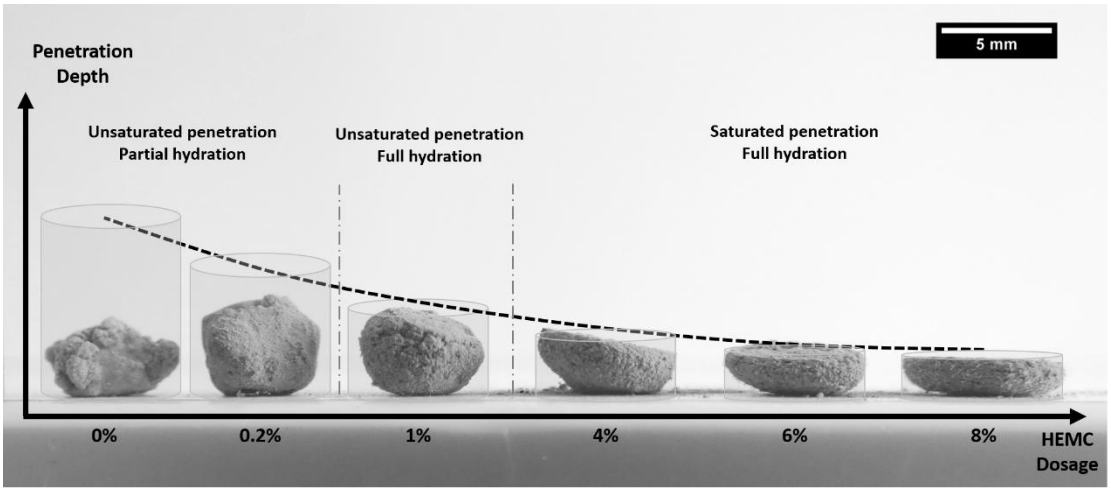

Fig. 11. *The morphology of the liquid penetrated area after hardening. The HEMC dosage is the mass ratio between HEMC and cement. The dash line stands for the expected stabilized penetration depth and the transparent cylinders stand for the expected stabilized penetration area.*

6. Conclusions

In this paper, we studied the physics behind net geometry control in the case of powder-based printing technologies.

We have measured one-dimensional water penetration as a function of time in simple experiments on various powder beds. Our results showed that water penetration goes through different penetration regimes. Initially, water saturates the powder bed and water penetration depth increases with the square root of time. This first regime is followed by an unsaturated penetration regime where penetration drastically slows down. Despite this slowing down, it was shown that water penetration does not stop when the porosity of the powder bed gets saturated as usually assumed. This results, on the typical time scale of cement setting, into an invaded porous zone larger than expected where the porosity is only partially saturated. It may, in turn, result into a loss of control of the resulting printed object geometry and into a poor hydration of the binder. Analysis and extrapolation have however suggested that this feature matters mostly when injecting a pure powder bed (i.e. with low packing properties and therefore high

porosity) with a low viscosity liquid.

In such cases, our second set of experiments has shown that dispersing a thickener inside the powder bed allows for a better control of the printed object net geometry and hydration. As water propagates into the powder under the effect of capillary suction, the thickener dissolves into the liquid and modifies its rheological behavior. Our results suggested that this may lead, for sufficient thickener dosages, to the formation of a yield stress fluid between the powder grains. This yield stress is then able to compete with capillary suction. Even at low thickener dosages, a yield stress eventually develops as the desaturation of the powder bed increases the effective thickener concentration. The formation of this non-Newtonian fluid between the powder grains allows, in turn, for the control of the naturally uncontrolled capillary-driven liquid penetration of the powder-bed.

References

[1] J. Pegna, Exploratory investigation of solid freeform construction, Autom. Constr. (1997). doi:10.1016/S0926-5805(96)00166-5.

[2] J. Pegna, Application of Cementitious Bulk Materials to Site Processed Freeform Construction, SFF Symp. (1995).

[3] T. Wangler, N. Roussel, F.P. Bos, T.A.M. Salet, R.J. Flatt, Digital Concrete: A Review, Cem. Concr. Res. 123 (2019) 105780. doi:10.1016/j.cemconres.2019.105780.

[4] E. Keita, H. Bessaies-Bey, W. Zuo, P. Belin, N. Roussel, Weak bond strength between successive layers in extrusion-based additive manufacturing: measurement and physical origin, Cem. Concr. Res. 123 (2019) 105787. doi:10.1016/j.cemconres.2019.105787.

[5] L. Reiter, T. Wangler, N. Roussel, R.J. Flatt, The role of early age structural build-up in digital fabrication with concrete, Cem. Concr. Res. 112 (2018) 86–95. doi:10.1016/j.cemconres.2018.05.011.

[6] D. Lowke, E. Dini, A. Perrot, D. Weger, C. Gehlen, B. Dillenburger, Particle-bed

519 3D printing in concrete construction – Possibilities and challenges, Cem. Concr.
520 Res. 112 (2018) 50–65. doi:10.1016/j.cemconres.2018.05.018.
521 [7] N. Roussel, Rheological requirements for printable concretes, Cem. Concr. Res.
522 112 (2018) 76–85. doi:10.1016/j.cemconres.2018.04.005.
523 [8] D. Marchon, S. Kawashima, H. Bessaies-Bey, S. Mantellato, S. Ng, Hydration
524 and rheology control of concrete for digital fabrication: Potential admixtures
525 and cement chemistry, Cem. Concr. Res. 112 (2018) 96–110.
526 doi:10.1016/j.cemconres.2018.05.014.
527 [9] G. De Schutter, K. Lesage, V. Mechtcherine, V. Naidu, G. Habert, I. Agusti-juan,
528 Cement and Concrete Research Vision of 3D printing with concrete —
529 Technical , economic and environmental potentials, Cem. Concr. Res. 112
530 (2018) 25–36. doi:10.1016/j.cemconres.2018.06.001.
531 [10] R.A. Buswell, W.R.L. da Silva, F.P. Bos, H.R. Schipper, D. Lowke, N. Hack, H.
532 Kloft, V. Mechtcherine, T. Wangler, N. Roussel, A process classification
533 framework for defining and describing Digital Fabrication with Concrete, Cem.
534 Concr. Res. 134 (2020). doi:10.1016/j.cemconres.2020.106068.
535 [11] A. Pierre, D. Weger, A. Perrot, D. Lowke, Penetration of cement pastes into
536 sand packings during 3D printing: analytical and experimental study, Mater.
537 Struct. Constr. 51 (2018) 22. doi:10.1617/s11527-018-1148-5.
538 [12] D. Weger, A. Pierre, A. Perrot, T. Kränkel, D. Lowke, C. Gehlen, Penetration of
539 Cement Pastes into Particle-Beds: A Comparison of Penetration Models,
540 Materials (Basel). 14 (2021) 389. doi:10.3390/ma14020389.
541 [13] D. Weger, C. Gehlen, Particle-Bed Binding by Selective Paste Intrusion—
542 Strength and Durability of Printed Fine-Grain Concrete Members, Materials
543 (Basel). 14 (2021) 586. doi:10.3390/ma14030586.
544 [14] D. Lowke, D. Talke, I. Dressler, D. Weger, C. Gehlen, C. Ostertag, R. Rael,
545 Cement and Concrete Research Particle bed 3D printing by selective cement
546 activation – Applications , material and process technology, Cem. Concr. Res.
547 134 (2020) 106077. doi:10.1016/j.cemconres.2020.106077.
548 [15] D. Weger, D. Baier, A. Straßer, S. Prottung, T. Kränkel, A. Bachmann, C. Gehlen,

549 M. Zäh, Reinforced Particle-Bed Printing by Combination of the Selective Paste
550 Intrusion Method with Wire and Arc Additive Manufacturing – A First
551 Feasibility Study, in: RILEM Bookseries, Springer, 2020: pp. 978–987.
552 doi:10.1007/978-3-030-49916-7_95.
553 [16] V. Voney, P. Odaglia, C. Brumaud, B. Dillenburger, G. Habert, From casting to
554 3D printing geopolymers: A proof of concept, Cem. Concr. Res. 143 (2021).
555 doi:10.1016/j.cemconres.2021.106374.
556 [17] P. Feng, X. Meng, J.F. Chen, L. Ye, Mechanical properties of structures 3D
557 printed with cementitious powders, Constr. Build. Mater. 93 (2015) 486–497.
558 doi:10.1016/j.conbuildmat.2015.05.132.
559 [18] P. Shakor, J. Sanjayan, A. Nazari, S. Nejadi, Modified 3D printed powder to
560 cement-based material and mechanical properties of cement scaffold used in
561 3D printing, Constr. Build. Mater. 138 (2017) 398–409.
562 doi:10.1016/j.conbuildmat.2017.02.037.
563 [19] M. V. Chubynsky, K.I. Belousov, D.A. Lockerby, J.E. Sprittles, Bouncing off the
564 Walls: The Influence of Gas-Kinetic and van der Waals Effects in Drop Impact,
565 Phys. Rev. Lett. 124 (2020). doi:10.1103/PhysRevLett.124.084501.
566 [20] S.L. Cormier, J.D. McGraw, T. Salez, E. Raphaël, K. Dalnoki-Veress, Beyond
567 tanner's law: Crossover between spreading regimes of a viscous droplet on an
568 identical film, Phys. Rev. Lett. 109 (2012).
569 doi:10.1103/PhysRevLett.109.154501.
570 [21] M. Xia, B. Nematollahi, J. Sanjayan, Printability, accuracy and strength of
571 geopolymer made using powder-based 3D printing for construction
572 applications, Autom. Constr. 101 (2019) 179–189.
573 doi:10.1016/j.autcon.2019.01.013.
574 [22] M. Xia, J. Sanjayan, Method of formulating geopolymer for 3D printing for
575 construction applications, Mater. Des. 110 (2016) 382–390.
576 doi:10.1016/j.matdes.2016.07.136.
577 [23] S. Fereshtenejad, J.J. Song, Fundamental study on applicability of powder-
578 based 3D printer for physical modeling in rock mechanics, Rock Mech. Rock

579 Eng. 49 (2016) 2065–2074. doi:10.1007/s00603-015-0904-x.
580 [24] P. Shakor, S. Nejadi, G. Paul, J. Sanjayan, Dimensional accuracy, flowability,
581 wettability, and porosity in inkjet 3DP for gypsum and cement mortar
582 materials, Autom. Constr. 110 (2020) 102964.
583 doi:10.1016/j.autcon.2019.102964.
584 [25] M. Asadi-Eydivand, M. Solati-Hashjin, A. Farzad, N.A. Abu Osman, Effect of
585 technical parameters on porous structure and strength of 3D printed calcium
586 sulfate prototypes, Robot. Comput. Integr. Manuf. 37 (2016) 57–67.
587 doi:10.1016/j.rcim.2015.06.005.
588 [26] C. Brumaud, H. Bessaies-Bey, C. Mohler, R. Baumann, M. Schmitz, M. Radler, N.
589 Roussel, Cellulose ethers and water retention, Cem. Concr. Res. 53 (2013)
590 176–184. doi:10.1016/j.cemconres.2013.06.010.
591 [27] J.W. Bullard, H.M. Jennings, R.A. Livingston, A. Nonat, G.W. Scherer, J.S.
592 Schweitzer, K.L. Scrivener, J.J. Thomas, Mechanisms of cement hydration, Cem.
593 Concr. Res. 41 (2011) 1208–1223. doi:10.1016/j.cemconres.2010.09.011.
594 [28] C. Clasen, W.M. Kulicke, Determination of viscoelastic and rheo-optical
595 material functions of water-soluble cellulose derivatives, Prog. Polym. Sci. 26
596 (2001) 1839–1919. doi:10.1016/S0079-6700(01)00024-7.
597 [29] W.W. Graessley, R.L. Hazleton, L.R. Lindeman, The Shear-Rate Dependence of
598 Viscosity in Concentrated Solutions of Narrow-Distribution Polystyrene, Trans.
599 Soc. Rheol. 11 (1967) 267–285. doi:10.1122/1.549089.
600 [30] E.W. Washburn, The dynamics of capillary flow, Phys. Rev. 17 (1921) 273–283.
601 doi:10.1103/PhysRev.17.273.
602 [31] J. Kozeny, Uber kapillare Leitung der Wasser in Boden, Sitzungsber. Akad. Wiss.
603 Wien. 136 (1927) 271– 306. https://ci.nii.ac.jp/naid/10029440086/ (accessed
604 December 19, 2019).
605 [32] P.C. Carman, Permeability of saturated sands, soils and clays, J. Agric. Sci. 29
606 (1939) 262–273. doi:10.1017/S0021859600051789.
607 [33] F. Osselin, A. Fabbri, T. Fen-Chong, J.M. Pereira, A. Lassin, P. Dangla,
608 Experimental investigation of the influence of supercritical state on the

relative permeability of Vosges sandstone, Comptes Rendus - Mec. 343 (2015) 495–502. doi:10.1016/j.crme.2015.06.009.

[34] I. Chatzis, F.A.L. Dullien, Modelling Pore Structure By 2-D And 3-D Networks With ApplicationTo Sandstones, J. Can. Pet. Technol. 16 (1977). doi:10.2118/77-01-09.

[35] A. Perrot, D. Rangeard, V. Picandet, S. Serhal, Effect of coarse particle volume fraction on the hydraulic conductivity of fresh cement based material, Mater. Struct. Constr. 48 (2015) 2291–2297. doi:10.1617/s11527-014-0311-x.

[36] A. Perrot, D. Rangeard, Effects of mix design parameters on consolidation behaviour of fresh cement-based materials, Mater. Struct. Constr. 50 (2017). doi:10.1617/s11527-016-0988-0.

[37] T. Chevalier, C. Chevalier, X. Clain, J.C. Dupla, J. Canou, S. Rodts, P. Coussot, Darcy's law for yield stress fluid flowing through a porous medium, J. Nonnewton. Fluid Mech. 195 (2013) 57–66. doi:10.1016/j.jnnfm.2012.12.005.

[38] F. Lequeux, L. Talini, E. Verneuil, G. Delannoy, P. Valois, Wetting of polymers by their solvents, Eur. Phys. J. E. 39 (2016) 1–9. doi:10.1140/epje/i2016-16012-y.

[39] S.R. Bonney, H.H. Rmaile, Process of making cold-water dispersible cellulose ethers and uses thereof, US 20070175361A1, 2007.